Advances in Geo-Energy Research

Vol. 15, No. 2, p. 112-128, 2025

Original article

A new near-wellbore modeling method for deviated wells in corner-point grid

Junjian Li[1]*, Lin Zhao[2], Olav Møyner[3], Knut-Andreas Lie[3]

[1]*State Key Laboratory of Petroleum Resources and Engineering, China University of Petroleum (Beijing), Beijing 102249, P. R. China*
[2]*Department of Exploration and Development, CNOOC Research Institute Co., Ltd, Beijing 100027, P. R. China*
[3]*Mathematics and Cybernetics, SINTEF Digital, Oslo 0314, Norway*

Keywords:
Near-wellbore modeling
deviated wells
hybrid grid
unstructured grid

Cited as:
Li, J., Zhao, L., Møyner, O., Lie, K. -A. A new near-wellbore modeling method for deviated wells in corner-point grid. Advances in Geo-Energy Research, 2025, 15(2): 112-128.
https://doi.org/10.46690/ager.2025.02.04

Abstract:
This paper presents the construction of a high-quality, robust hybrid grid for near-wellbore modeling in the vicinity of a deviated well. The far-field region is modeled using a corner-point grid, while the near-wellbore region-referred to as the volume of interest-is remeshed using a layered unstructured grid, which consists of a combination of Voronoi and radial sub-grids. A detailed gridding and simulation workflow is outlined. The construction of the novel layered unstructured grid begins with building a base surface grid on the surface typically aligned to middle well point. The grids on the other surfaces are built through preserving the base topology but adjusting the nodes of base grid to fit the well points deviating from the base well point. A flow-based node rearrangement method is proposed to adjust the grid nodes to gain high-quality grids on each surface. The positions of new nodes are determined by ensuring equal streamlines and pressure values between nodes on the base and target surfaces, improving grid orthogonality as streamlines remain perpendicular to equipotential lines. The method's ability to generate high-quality grids for deviated wells is demonstrated through illustrative and validation examples. Computational performance is assessed through direct comparisons across three case studies, showing that the new near-wellbore modeling model provides accurate well solutions and pressure maps with a reasonable computational cost. Additionally, the near-wellbore modeling model outperforms standard models in capturing gas flow with high compressibility, describing flow behavior in heterogeneous reservoirs, and predicting production parameters in multilayer systems.

1. Introduction

Reservoir simulation has long been a crucial tool for predicting well production and analyzing flow dynamics due to its ability to accurately capture reservoir geology, rock properties, flow physics, and well controls (Aziz and Settari, 1979; Lie et al., 2012, 2019; Zhao et al., 2020). The corner-point grid (CPG) format has become the industry standard for reservoir grid models (Ponting, 1989; GeoQuest, 2021). The CPG framework is established using a set of vertical or inclined pillars, with each hexahedral cell bounded by four pillars. The depth coordinates along these pillars define the corners of the cells, allowing precise grid generation (Lie, 2019). This makes the CPG particularly well-suited for representing the spatial structure of stratigraphic layers and complex fault systems.

Well modeling describes the interaction between well connections and reservoir grid cells, and thus directly influences the accuracy of predicted well solutions (Zhao et al., 2018). Standard well models use a source term to represent flow in and out of well cells, i.e., reservoir grid cells traversed by virtual well segments. This approach is computationally efficient

Yandy Scientific Press

*Corresponding author.
E-mail address: junjian@126.com (J. Li); zhaolin11@cnooc.com.cn (L. Zhao); olav.moyner@sintef.no (O. Møyner); Knut-Andreas.Lie@sintef.no (K. -A. Lie).

Received October 21, 2024; revised November 18, 2024; accepted December 17, 2024; available online December 23, 2024.

as it avoids the need for additional gridding. In well modeling, the flow between the wellbore and reservoir grid cells is calculated using a well index, which relates the pressure difference to the flow rate. The reservoir flow is linear, while flow toward the wellbore is radial. An equivalent radius, r_{eq}, bridges these flow regimes, allowing for a consistent inflow/outflow calculation through the well index. Numerous works have focused on estimating this equivalent radius. Peaceman (1978) proposed that for Cartesian grid with square cells and isotropic permeability, $r_{eq} \approx 0.2\Delta x$, based on numerical experiments and an approximate analytical approach. This formula was later extended by Peaceman (1983) to accommodate rectangular cells and anisotropic permeability. This formula has been accepted by mainstream simulators. Further studies addressed more complex scenarios, including off-center wells (Abou-Kassem and Aziz, 1985; Su, 1995), off-center and multiple wells within a single cell (Peaceman, 1990), unstructured grids (Ding et al., 1998), partially perforated well (Dogru, 2010a, 2010b), and discrete fracture models (Zhao et al., 2018).

For large-scale flow scenarios, the standard well model is a suitable choice (Ding et al., 2014). However, when high-resolution modeling of near-wellbore flow is required, such as for water control operations, the standard model falls short in several ways. First, the modeled well trajectory often appears zig-zagged due to the alignment of well segments with the grid's cell orientations, particularly in the case of deviated wells. Additionally, coarse grid cells cannot capture rock properties with sufficient resolution, and the hexahedral grid geometry, optimized for linear flow, is inadequate for representing the radial flow characteristic of the near-wellbore region. Although Cartesian local grid refinement (Rosenberg, 1982; Ding, 2011; Hoteit and Chawathé, 2016; GeoQuest, 2021) can improve resolution, it introduces a large number of additional cells and poses challenges for convergence. Moreover, Peaceman's model imposes a lower limit on the refined cell size, $\Delta x > 5r_w$ (for isotropic, square cells), which restricts the achievable resolution.

The near-wellbore model (NWM) proposed herein is specifically designed for high-resolution flow description in the vicinity of wells. It employs a hybrid grid that includes a radial component to accurately represent the radial flow geometry around the wellbore, allowing for explicit gridding of the circular wellbore. Currently, NWM grids can be categorized into three types: Structured hybrid grids, tetrahedral grids, and layered unstructured hybrid grids.

Pedrosa and Aziz (1986) identified that source models become invalid during periods of rapid saturation changes in the near-wellbore region. In response, they introduced a structured hybrid grid system that replaces the near-wellbore corner-point cells with a single-column radial grid. Building on this foundation, Ewing et al. (1989) expanded the model's application scenarios, while Krogstad and Durlofsky (2009) developed a radial hybrid grid specifically for horizontal wells. The industry-standard simulator ECLIPSE has incorporated this model through the RADFIN keyword (GeoQuest, 2021). Although this method offers simplicity in gridding and is computationally efficient, it still struggles to accurately represent a real well trajectory due to the radial grid's alignment with the CPG cells.

Unstructured hybrid grids utilize fully three-dimensional (3D) unstructured grids to connect the corner-point and the radial grids. These 3D grids can, for instance, be generated using the 3D power diagram method (Flandrin et al., 2004, 2006). Bennis et al. (2006, 2008) improved Flandrin's method from Cartesian to corner-point grids through a nonlinear transformation function. Mouton et al. (2009, 2010) further enhanced this transformation function to improve grid quality for highly deformed corner-point cells. This method offers significant flexibility in modeling complex well trajectories, supporting vertical, slant, and horizontal wells. However, the use of an unstructured grid can disrupt the stratigraphic layering that reservoir engineers prioritize, and assigning rock properties to the cells can be challenging.

Layered unstructured hybrid grids employ a 2.5D unstructured grid to connect the CPG and the radial grid, where the grids in the x-y plane are unstructured while maintaining a consistent topological structure across each layer. This approach preserves stratigraphic layering, allowing for straightforward assignment of rock properties on a layer-by-layer basis. As such, this gridding strategy may be the most suitable method for near-wellbore modeling. ECLIPSE has implemented such a grid in a module named NWM (GeoQuest, 2021), which offers several types of unstructured grid geometry, including rectangular, uniform hexagonal, radial, and others (see Fig. S1 in Supplementary file). The module can produce high-quality grids for vertical wells and slightly deviated wells. However, grid quality deteriorates significantly when dealing with highly inclined deviated wells, leading to the generation of improper cells around the radial grid, which can produce incorrect results (see Fig. S1 in Supplementary file).

This paper aims to establish a high-quality and robust layered unstructured hybrid grid for near-wellbore modeling of deviated wells. Gridding and simulation are conducted using the open-source software MRST (Lie et al., 2012, 2019; Krogstad et al., 2015). The paper is organized as follows: Section 2 introduces pertinent flow equations, while Section 3 covers the foundational concepts of gridding. Section 4 details the gridding workflow, emphasizing a flow-based method for constructing a high-quality unstructured grid for deviated wells. Section 5 discusses computational of transmissibility adapted to various flow geometries, while Section 6 presents several simulation examples.

2. Flow equations

For simplicity, this paper considers an oil–water flow model which describes a two-phase (oleic and aqueous), two-component (oil and water) fluid flow system. The discretized mass conservation for component α is given by (Lie et al., 2012, 2019; Zhao et al., 2018):

$$\frac{V_{\phi i}}{dt}\left[\left(\frac{S_\alpha}{B_r B_\alpha}\right)_i^{n+1} - \left(\frac{S_\alpha}{B_r B_\alpha}\right)_i^{n}\right] + \sum_{j\in\eta_c} \lambda_{\alpha ij} T_{ij}\left[(p_{\alpha i} - p_{\alpha j}) - \rho_{\alpha ij} g\left(z_i - z_j\right)\right] + \lambda_{\alpha i} W I_i\left[(p_{\alpha i} - p_{bh}) - \rho_{\alpha i} g\left(z_i - z_{ref}\right)\right] = 0 \quad (1)$$

where V_ϕ denotes pore volume, B_r denotes rock-volume factor, λ denotes mobility, T is face transmissibility, p is pressure at cell center, ρ is density, z is depth at cell center, WI is well index, and z_{ref} is reference depth. Assembling the discrete equations for each component in every grid cell, the non-linear system of equations is constructed upon a reservoir grid domain. The nonlinear system in is solved by Newton-type iteration, for which the Jacobian is calculated by automatic differentiation technique, which in conjunction with the discrete operators facilitate rapid prototyping capability (Krogstad et al., 2015; Wang and Shahvali, 2016; Lie, 2019).

3. Gridding foundations

The hybrid NWM grid is generated by the MRST grid factory, which offers a uniform grid representation and a library of routines for constructing a wide variety of grids while computing the necessary geometric information (Lie et al., 2012, 2019). The NWM grid consists of two types of sub-grids: the semi-structured CPG and the layered unstructured grid.

The corner-point grids are constructed using the built-in processor of MRST. The two-dimensional (2D) unstructured grids are generated by a tessellation grid generator, which can theoretically produce any type of 2D grid by accepting a point set described by a connectivity list and geometric coordinates. Layered grid (2.5D) are created using a layered grid generator that accepts a set of surface grids aligned vertically in a topological manner. The surface grid serves as a spatial representation of the 2D grid, with nodes that include z-coordinates.

4. Gridding workflow

4.1 Volume of interest

The near-well region, referred to as the volume of interest (VOI), is reconstructed by a layered unstructured grid to provide a high-resolution description of near-well flow. The VOI is defined by a user-specified polygon, and actual VOI boundary is clipped by the cell edges (see Fig. S2 in Supplementary file). The VOI encompasses all active CPG layers to prevent non-matching intersections between the two different grid geometries. The CPG objects within the VOI are extracted to serve as constraints for the layered unstructured grid.

4.2 Base 2D unstructured grid

Due to the differing well points on the VOI surfaces for a deviated well, the base 2D unstructured grid is initially constructed on the base VOI surface, typically the middle surface. Subsequent 2D grids for each VOI surface are derived from this base grid. The base 2D unstructured grid consists of two sub-grids: a radial sub-grid and a Voronoi sub-grid.

The radial sub-grid is designed to capture the radial flow in the well vicinity (see Fig. S3 in Supplementary file). In this arrangement, the nodes of the radial grid are organized into concentric circles aligned at various angles. Consequently, these circles are approximated by regular polygons, with the innermost circle representing the wellbore. The radial node distribution can be logarithmic or uniform.

The Voronoi sub-grid serves to connect the radial sub-grid with the outer CPG, existing within the region defined by the VOI boundary and the radial sub-grid boundary. This Voronoi grid exhibits excellent orthogonality, which is generated by clipping the Voronoi diagram derived from a set of generating points (or sites) (Wang and Shahvali, 2016; Berge et al., 2019).

The generating points given as input to a Voronoi diagram generator are the centers of the Voronoi cells, not the nodes themselves. Consequently, fixed points on the two boundaries cannot be directly included in the generating point set. This creates challenges in point design, as it necessitates placing several auxiliary generating points around the boundaries to accurately reproduce the fixed boundary points that function as the nodes of the Voronoi cells. In this context, we discuss two types of auxiliary generating points tailored to different boundary geometries.

Since the radial sub-grid boundary is a regular polygon, the auxiliary points can be computed directly. To generate a specific boundary point, four auxiliary points are required. The line segment connecting a pair of auxiliary points serves as the perpendicular bisector of an edge associated with the boundary point, and vice versa (see Fig. S4 in Supplementary file). The distances from the boundary point to the four auxiliary points are equal, making these points concyclic, with the circle centered at the boundary point. Following this principle, the auxiliary points form two regular polygons, with their vertices staggered relative to the boundary points.

The VOI boundary polygon is typically irregular and concave, making the direct computation of auxiliary points challenging based solely on the polygon's information. To address this, the centers of the CPG faces-comprising boundary x-y faces and those outside the VOI-are incorporated into the generating point set. The x-y faces of a CPG generally have regular shapes, with their four vertices often being nearly concyclic. As a result, the original CPG x-y face geometry can be effectively reproduced in Voronoi style using this generating point set, which includes the face centers (see Fig. S5 in Supplementary file). Consequently, the VOI boundary nodes can be identified by tracing the Voronoi nodes, which closely overlap or are in proximity to the VOI boundary nodes.

The main generating points are positioned within the region enclosed by the polygon formed by the centers of the boundary x-y CPG faces and the outer auxiliary polygon for the radial grid boundary. A high-quality point set is generated using the distmesh software, which employs a mechanical analogy between a triangle mesh and a 2D truss to iteratively optimize point placement (Persson and Strang, 2004; Persson, 2005). In this approach, the triangle edge length gradually increases from the inner polygon to the outer polygon through a scaled length function (see Fig. S6 in Supplementary file).

The Voronoi diagram is generated from a set of three types of points (see Fig. S7 in Supplementary file). To create a suitable Voronoi grid, the Voronoi diagram should be clipped and the overlapping points should be merged. The target 2D unstructured grid is constructed by integrating the Voronoi sub-grid and the radial sub-grid (see Fig. S7 in Supplementary file).

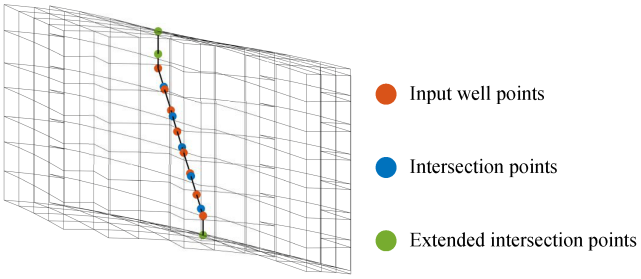

Fig. 1. 3D well trajectory and three types of well points.

4.3 2D unstructured grids for all surfaces

4.3.1 Well trajectory treatment

The well trajectory is defined by a set of discrete 3D well points that divide the well into several segments. These points can be derived from well survey and logging data, depending on the required accuracy for trajectory and permeability descriptions. It is crucial to include intersection points between the well trajectory and VOI surfaces in the well-point set to prevent non-matching faces between the CPG and unstructured grid in the layer dimension (see Fig. 1). Additionally, the well trajectory should be extended if it does not cover all active CPG layers to ensure alignment in the surface dimension (see Fig. 1). Original input properties for each segment, such as permeability, skin factor, and open/shut flag, are then mapped onto the new segments.

4.3.2 Grid nodes rearrangement

Each well point corresponds to a VOI surface, where the intersection point aligns with the CPG surface, and the input well point is placed on the new surface between CPG layers. The 2D unstructured grid on each VOI surface is derived from the base 2D unstructured grid. Since the layered unstructured grid consists of surface grids aligned vertically, the 2D grids on all VOI surfaces share the connectivity list of the base 2D grid. The grid nodes on each surface are rearranged based on the node placement from the base grid, considering the boundary nodes and well points specific to each surface. This rearrangement of nodes is categorized into two types based on the sub-grid type.

The radial sub-grid nodes maintain their ring arrangement in a regular polygon to accurately describe radial flow near the wellbore. To achieve this, a linear movement is applied by imposing an offset on all radial sub-grid nodes. This offset is calculated as the difference between the coordinates of the well point on the target VOI surface and those on the base surface (see Fig. S8 in Supplementary file).

The Voronoi sub-grid nodes on the target surface undergo nonlinear movement because the VOI boundary and radial sub-grid boundary shift differently between the target and base surfaces. The key to achieving high grid quality lies in the appropriate placement of the new Voronoi nodes on the target surface. One effective method is to perform 2D interpolation, using the boundary nodes as sample points and the differences in x/y coordinates between the two surfaces as sample values. The query points are the Voronoi nodes on the base surface, and the nodes on the target surface are obtained by adding the interpolated values to these query points (see Fig. 2). This process shows significant deformation of the Voronoi sub-grid on the target surface, particularly near the radial sub-grid boundary, which may negatively impact computational accuracy.

A flow-based node arrangement method is proposed for placing new nodes. This method utilizes two-component flow parameters-stream and pressure-to define a 2D node position within the Voronoi region, which features two constant-pressure boundaries. Consequently, a node can be determined by the intersection of a streamline and an isopiestic line (see Fig. 3). The new nodes on the target surface are computed to maintain the equality of both stream and pressure between each node on the target surface and its corresponding node on the base surface. This approach enhances grid orthogonality, as the streamline is perpendicular to the isopiestic line.

The implementation of the new method begins by numerically solving for the stream and pressure at the base Voronoi nodes. To facilitate this, a fine, evenly spaced Cartesian grid is constructed within the Voronoi region on the base surface (see Fig. S9 in Supplementary file). Notably, the outer boundary is defined by the polygon formed by the centers of the boundary x-y CPG faces, rather than the VOI boundary polygon. This adjustment improves the orthogonality of the cells near the outer boundary (see Fig. S9 in Supplementary file). The property model is assumed to be homogeneous, and the flow is single-phase and incompressible. The boundary pressure equals to 0 for the outer boundary and 1 for the inner boundary, respectively. Pressures at Voronoi nodes are computed using 2D interpolation.

Streamlines are used to express stream function. Using the flux field computed from the pressures on the Cartesian grid, streamlines are traced by Pollock's algorithm (Pollock, 1988), which employs a linear velocity, based on the assumption that each velocity component within a cell varies linearly and is independent of the others.

The next step involves reconstructing the fine Cartesian grid and computing the incompressible pressure on the target surface. Following this, the streamlines corresponding to those on the base surface are calculated. The pressures along each streamline are obtained through 2D interpolation, using Cartesian grid cell centers as sample points and discrete streamline points as query points. Finally, the Voronoi nodes on the target surface are identified along the streamlines, ensuring that the pressures at these nodes are equal on both surfaces. This can be achieved by performing repeated 1D pressure-coordinate interpolations for each streamline.

A key step in the process is tracing streamlines on the target surface based on the information from the streamlines on the base surface. To maintain consistency in stream values, the forward streamlines on the target surface originate from their corresponding starting points on the inner boundary of the base surface. However, due to the differing relative locations of the two boundaries between the surfaces, these streamlines can accurately represent radial flow in the near-well region but may deviate from their expected trajectories near the outer boundary, as illustrated in Fig. S10 in Supplementary file. T-

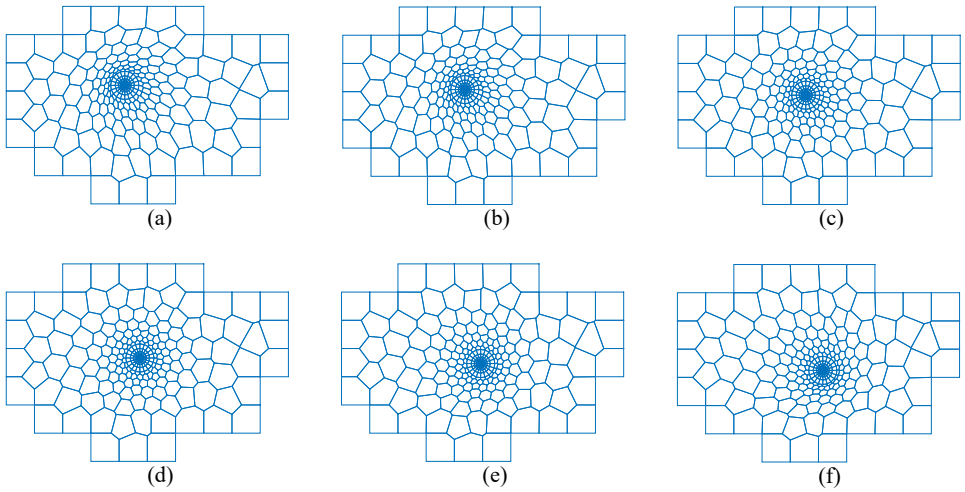

Fig. 2. 2D unstructured grid derived from the direct 2D interpolation method on different surface. (a) Top surface (2), (b) surface 3, (c) surface 4, (d) base surface (5), (e) surface 6 and (f) bottom surface (7).

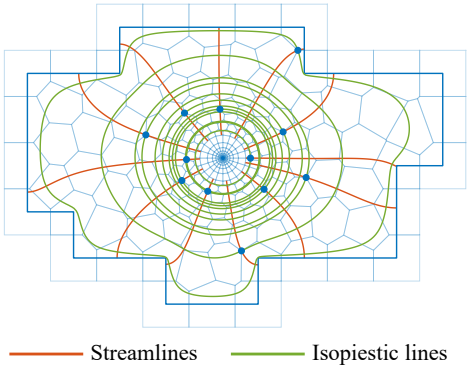

Fig. 3. Node positions expressed by the intersection of a streamline and an isopiestic line.

he streamlines are color-coded based on their starting angles relative to the well points. This visualization shows that, although streamlines starting from the same angle present similar trajectories in the near-well region for both surfaces, they terminate at different positions on the outer boundary. Consequently, the grid derived from this method exhibits good quality in the near-well region but poor quality near the outer boundary, as depicted in Fig. S10 in Supplementary file.

Similarly, starting backward streamlines from the corresponding termination points of base streamlines on the outer boundary can generate streamlines that accurately reflect linear flow in the vicinity of the outer boundary. However, these streamlines may deviate from their expected trajectories in the near-well region, as shown in Fig. S11 in Supplementary file. The backward streamlines are color-coded according to their starting angles relative to the center of the region. This representation illustrates that, for different surfaces, streamlines starting from the same angle exhibit similar trajectories in the vicinity of the outer boundary but terminate at different positions on the inner boundary. Consequently, the grid derived from this method demonstrates good quality near the outer boundary but exhibits poor quality in the near-well region, as depicted in Fig. S11 in Supplementary file.

To achieve better grid quality, a weighting method is proposed:

$$\boldsymbol{p} = f\boldsymbol{p_f} + (1-f)\boldsymbol{p_b}, \quad f = \frac{1}{(\alpha R)^n + 1} \tag{2}$$

where $\boldsymbol{p}$ is the weighted node coordinates, $\boldsymbol{p_f}$ is the node coordinates obtained from forward streamlines, and $\boldsymbol{p_b}$ is node coordinates obtained from backward streamlines. Furthermore, f denotes a weighting factor, α and n are constants, and R is defined as the ratio of the distance from the inner boundary to the distance from the outer boundary. The larger α and n are, the closer f is to 0, and the weighted nodes are closer to the nodes from backward streamline. According to numerous tests, α ranging from 0.5 to 3, and n ranging from 1 to 3 will give good grid quality.

The combination of the new Voronoi nodes and the newly positioned radial nodes creates a set of nodes on the target surfaces, enabling the construction of 2D grids using these nodes along with the connectivity list from the base 2D grid. An example of the 2D grids across all surfaces is illustrated in Fig. 4, demonstrating high grid quality, even for surfaces that deviate significantly from the base surface. A factor is introduced to evaluate the grid quality quantitatively. The factor is computed by area-weighting included angles between the vector of face center towards cell center and face normal vector for all half-faces. A small factor means a higher overall grid orthogonality. The factor is reduced from 31 to 19 by the new method compared with the 2D interpolation method.

4.4 Layered unstructured grid

The 3D layered grid is constructed by connecting the surface grids to form a volumetric object. Each surface grid is non-volumetric, created by assigning z-coordinates to a 2D grid. These z-coordinates are determined through 2D interpolation, using the 3D coordinates of the CPG cell centers as the source. An example of the layered grid is presented in Fig. 5.

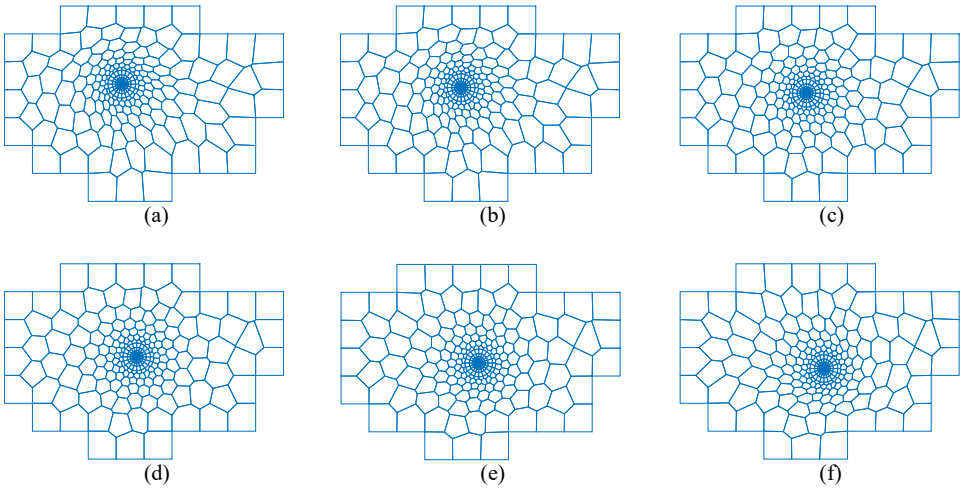

Fig. 4. 2D unstructured grid by the flow-based node arrangement method on different surfaces. (a) Top surface (2), (b) surface 3, (c) surface 4, (d) base surface (5), (e) surface 6 and (f) bottom surface (7).

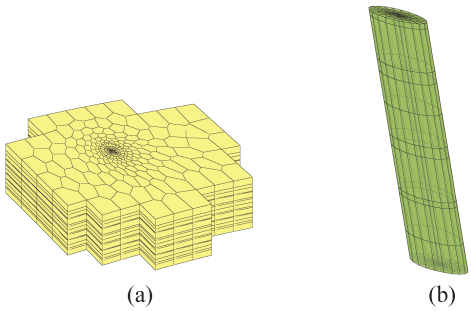

Fig. 5. Illustration of the layered unstructured grid and its radial sub part. (a) Layered unstructured grid and (b) radial sub-grid.

4.5 Hybrid NWM grid

The CPG cells within the VOI are removed, and the updated CPG is combined with the layered unstructured grid to form the hybrid NMW grid. For simplicity, this combination does not merge the boundary nodes from the two sub-grids in the grid domain, even though they are physically identical. Instead, in the computational domain, non-neighboring connections (NNCs) will be employed to restore the connections between the boundary cells of the two sub-grids. An example of the hybrid NWM grid is illustrated in Fig. 6.

The 2D distances from top well point to base well point and to the VOI boundary determine the capable scope of the new method. The ratio between the two distances is recommended to be not exceed than 0.4 through numerical experiments. For wells with large 2D lengths, one can choose to enlarge the VOI boundary or adopt the near-wellbore modeling algorithm for horizontal wells.

5. Transmissibility

The transmissibility for NMW grid face is calculated by the harmonic average of one-side half-transmissibilities associated with two neighboring cells. The half-transmissibility calculations can be categorized into three types, depending on the flow approximation and the geometry of the grid.

5.1 CPG

For the CPG, the linear flow approximation is employed. The permeability is defined within a local coordinate system, ensuring that the permeability direction aligns with the cell orientation. The half-transmissibility in the x-direction reads (GeoQuest, 2021):

$$t_{x1} = k_{x1} R_{ntg1} A \frac{\boldsymbol{D_1} \cdot \boldsymbol{n}}{\boldsymbol{D_1} \cdot \boldsymbol{D_1}} \tag{3}$$

where t_{x1}, k_{x1}, and R_{ntg1} denote half-transmissibility, x-permeability, and net-to-gross (NTG) ratio of cell 1, A is the face area, $\boldsymbol{D_1}$ is the distance vector from the cell center to the face center, and $\boldsymbol{n}$ is the face normal vector. The expression for t_{x2}, t_{y1}, and t_{y2} is analogous, and the NTG ratio is absent for t_{z1} and t_{z2}.

5.2 Layered unstructured grid

5.2.1 Voronoi sub grid

For the Voronoi component of the layered grid, the rock properties (permeability, porosity, and NTG) are derived through 2D interpolation. The centers of removed CPG cells act as sample points and the rock properties act as sample values. The query points are Voronoi cell centers. To preserve the stratigraphic feature of reservoir model, the 2D interpolations are repeated on every grid layers. For the scalar field, i.e., porosity and NTG, the interpolations are performed directly. For the permeability field, the coordinate system of the permeability definition per cell is transformed from the local one to the global one:

$$\left(k_{x,glo}, k_{y,glo}, k_{z,glo}\right) = k_{x,loc}\boldsymbol{d_x} + k_{y,loc}\boldsymbol{d_y} + k_{z,loc}\boldsymbol{d_z} \tag{4}$$

where $k_{x,glo}$ denotes x-permeability in global coordinate system that Voronoi sub grid adopts, and $k_{x,loc}$ denotes x-permeability in local coordinate system that CPG adopts, $\boldsymbol{d_x}$ is the unit distance vector between opposite x-face centers. $k_{y,glo}$,

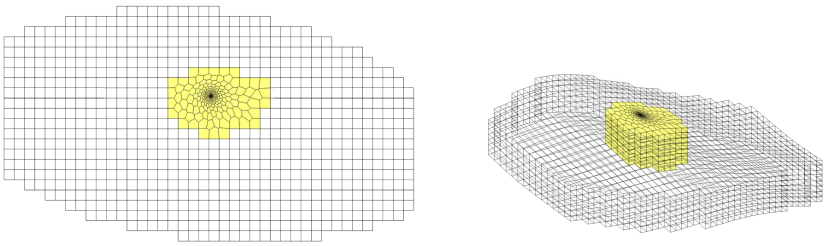

Fig. 6. Illustration of the hybrid NWM grid. (a) 2D and (b) 3D view.

$k_{z,glo}$, $k_{y,loc}$, $k_{z,loc}$, $\boldsymbol{d_y}$, and $\boldsymbol{d_z}$ are defined analogously.

Since the orientaions of the Voronoi cells are arbitrary, they may not align with the permeability direction. Consequently, the lateral half-transmissibility is determined using the two-point flux approximation (TPFA) scheme:

$$t_1 = R_{tng1} A \frac{\boldsymbol{D_1} \times \boldsymbol{K_1} \cdot \boldsymbol{n}}{\boldsymbol{D_1} \cdot \boldsymbol{D_1}} \tag{5}$$

where $\boldsymbol{K_1}$ is the permeability vector with off-diagonal terms omitted in a permeability tensor. Also, the NTG ratio is absent for vertical transmissibility.

5.2.2 Radial sub grid

For the radial component of the layered grid, the rock properties are explicitly defined based on well logging data or through 2D interpolations, like the Voronoi component. A radial flow approximation is employed to enhance the accuracy of flow descriptions near the wellbore. Pedrosa and Aziz (1986) introduced formulas for radial and angular transmissibility tailored for a pure circular radial grid system, considering both regularly annular-sector cells and non-annular-sector cells along the border. Since the radial sub-grid uses regular polygons to approximate circles, and the annular-sector cells are represented as trapezoidal cells, the formulas for non-annular-sector cells are applied. In this context, each trapezoidal cell is substituted with a fictitious annular-sector cell that shares the same volume and rock properties as the original cell, as illustrated in Fig. S12 in Supplementary file. The radius of the apparent circle is computed based on the node coordinates according to Eq. (6):

$$r_j = R_j \sqrt{\frac{n_\theta}{2\pi} \sin\frac{2\pi}{n_\theta}}, \quad j = 1, 2, \cdots, n_r + 1 \tag{6}$$

where r_j is the radius of the j^{th} apparent circle. Then, the radial and angular half-transmissibilities can be given by:

$$t_{r1} = \frac{2\pi k_r \Delta z R_{ntg}}{n_\theta \ln \frac{r_{cj}}{r_j}}, \quad t_{r2} = \frac{2\pi k_r \Delta z R_{ntg}}{n_\theta \ln \frac{r_{j+1}}{r_{cj}}} \tag{7}$$

$$t_{\theta 1} = t_{\theta 2} = \frac{n_\theta k_\theta \Delta z R_{ntg}}{\pi} \ln \frac{r_{j+1}}{r_j} \tag{8}$$

where k_r and k_θ are radial and angular permeability, respectively, Δz is the cell thickness, and r_{cj} is the radius of the cell center, which is computed by the integral of steady-state pressure within the cell:

$$r_{cj} = r_j \exp\left(\frac{\alpha^2}{\alpha^2 - 1} \ln\alpha - \frac{1}{2}\right), \quad \alpha = \frac{r_{j+1}}{r_j} \tag{9}$$

The vertical flow is still based on linear approximation, and t_{z1} and t_{z2} are computed by Eq. (5) without NTG ratio.

Although the wellbore is explicitly modeled using the innermost polygon, the standard Peaceman well equation framework is compatible with the boundary well model. In this framework, the well cells are represented as the innermost cells, and the well indices correspond to the half-transmissibilities of the wellbore faces.

5.3 Sub-grid coupling

As mentioned in Section 4.5, in the computational domain, non-neighboring connections (NNCs) will be utilized to restore the connections between the boundary cells of the two sub-grids. The NNCs, along with their associated transmissibilities, will be added after the grid neighborhood and transmissibility definitions. In this context, the NNCs correspond to the layered boundary cells of the two sub-grids. Notably, the boundary faces of the computational grid (CPG) may cover multiple boundary faces of the layered grid, as illustrated in Fig. 7. To address this, the CPG boundary faces are subdivided into sub-faces that match the boundary faces of the layered grid. The half-transmissibility of each sub-face is determined as a proportional area of the original half-transmissibility. Meanwhile, the half-transmissibilities of the boundary faces of the layered grid are preserved.

6. Simulation examples

6.1 2D grid performance

This section validates the computational accuracy of the 2D grids across different surfaces. The first case involves modeling a single-phase incompressible flow with a rectangular constant-pressure boundary and an off-center well. Analytical potential for this scenario can be derived using a combination of mirror reflection theory and the potential superposition law.

Three 2D grids are extracted from a layered unstructured grid, including the base 2D grid and two additional grids with well positions that deviate significantly from the base well position. All three grids feature an 80 m × 50 m rectangular boundary with a constant pressure of 10 MPa. The well production rate is set at 5 m^3/d, with a permeability of 0.01 μm^2 and a fluid viscosity of 1 mPa·s. Pressures are calculated using a single-phase incompressible flow solver.

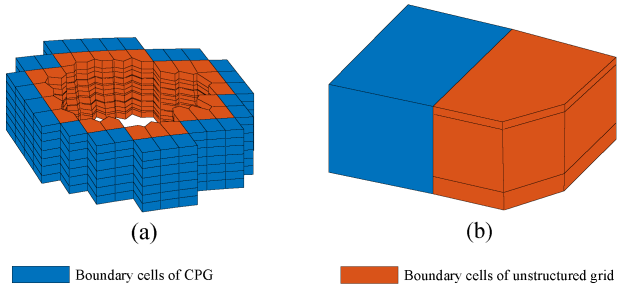

Fig. 7. Boundary cells of CPG and unstructured grids and their intersections. (a) All boundary cells and (b) part of boundary cells.

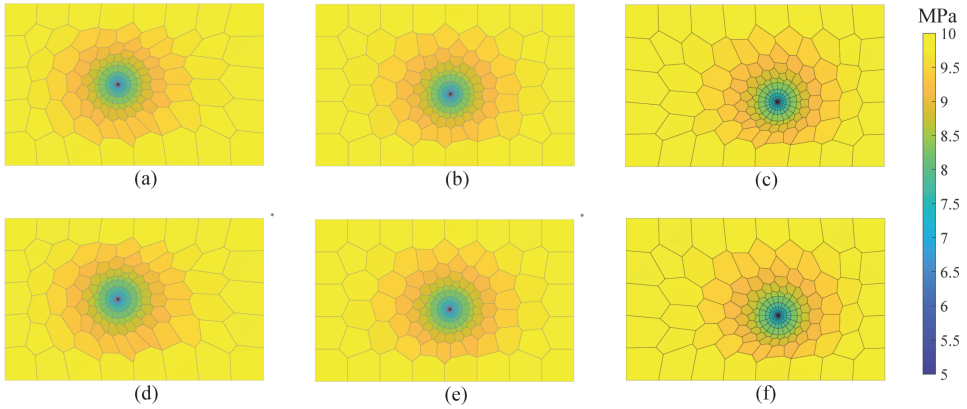

Fig. 8. Comparisons between analytical pressures and numerical pressures for incompressible flow. (a) Analytical, top surface (1), (b) analytical, base surface (5), (c) analytical, bottom surface (8), (d) numerical, top surface (1), (e) numerical, base surface (5) and (f) numerical, bottom surface (8).

Comparisons between analytical pressures and numerical pressures are presented in Fig. 8, indicating that the numerical pressures closely match the analytical values across all three grids. Furthermore, pressure contours computed through interpolation are illustrated in Fig. 9. The base grid demonstrates a high level of agreement between the numerical and analytical contours, while the other two grids also show commendable performance in these comparisons.

The second case examines a two-phase compressible flow featuring a complex boundary and an off-center well. The boundary supplies water at a constant pressure of 30 MPa, with a maximum water saturation of 0.7. The well operates at a constant flow rate of 10 m^3/d. As in the previous case, three 2D grids are extracted from a layered unstructured grid, comprising the base 2D grid and two additional grids with significant deviations from the base well position.

For reference, results are obtained from a fine Cartesian grid. This grid is clipped according to the boundary and adjusted to ensure that the well is positioned at the center of a cell, thereby satisfying the assumptions of the Peaceman well model. To avoid the well radius r_w exceeding the Peaceman equivalent radius of $0.2\Delta x$, the $x-$ and $y-$ cell sizes are set to $6r_w$.

In terms of fluid properties, the oil viscosity is 5 mPa·s, while water viscosity is 1 mPa·s. The oil, water, and rock compressibility are 6.7×10^{-3}, 4.3×10^{-4}, and 3×10^{-4} MPa^{-1}, respectively. The connate water saturation is 0.2, and residual oil saturation is 0.3.

The pressure, saturation, and well solutions are computed using an oil-water simulator. The resulting oil saturation maps are presented in Fig. 10. These maps illustrate that the boundary region near the well primarily supplies the water driving flow, while the remaining oil is located in the area between the well and the far-well boundary. The fine Cartesian grid produces a high-resolution oil saturation map, whereas the unstructured grid yields lower-resolution results because of grid cell size. However, both grids exhibit similar phenomena in oil distribution.

The oil rates and bottom hole pressures (BHPs) are shown in Fig. 11. The results indicate that, thanks to the high-resolution description provided by the radial sub-grid in the well vicinity, the oil rates and BHPs obtained from the unstructured grid closely match those from the fine Cartesian grid. This similarity demonstrates the computational accuracy of the well solution data.

6.2 A block model

In this section, the new method is validated using a block model featuring a deviated producer situated in the middle of the reservoir, along with two corner vertical injectors, as illustrated in Fig. 12. The dimensions of the model are 300 m $\times$ 300 m $\times$ 20 m, with horizontal permeability set at 0.1 μm^2 and vertical permeability at 0.01 μm^2. The porosity is 0.15.

Regarding the grids, the basic Cartesian grid has dimen-

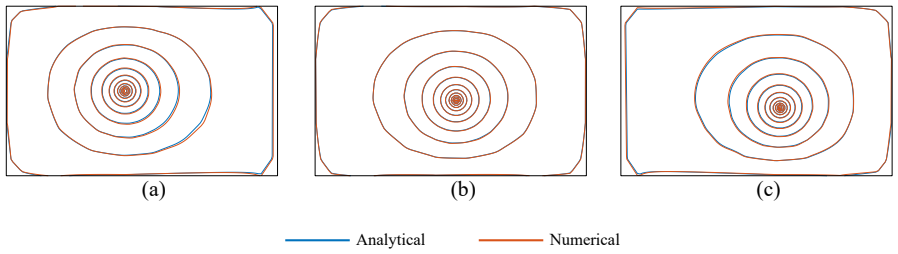

Fig. 9. Comparisons between analytical pressures and numerical pressures for incompressible flow. (a) Analytical, top surface (1), (b) analytical, base surface (5), (c) analytical, bottom surface (8), (d) numerical, top surface (1), (e) numerical, base surface (5) and (f) numerical, bottom surface (8).

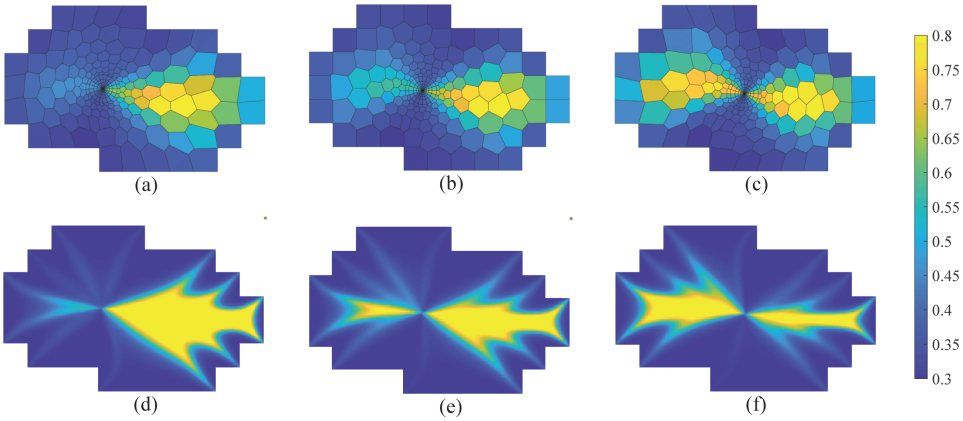

Fig. 10. Comparisons of oil saturations between unstructured grid and fine Cartesian grid for two-phase compressible flow at 40 day. (a) Unstructured grid, top surface (2), (b) unstructured grid, base surface (4), (c) unstructured grid, bottom surface (7), (d) reference grid, top surface (2), (e) reference grid, base surface (4) and (f) reference grid, bottom surface (7).

sions of $30 \times 30 \times 10$, resulting in a cell size of 10 m $\times$ 10 m $\times$ 2 m. The wells are designed to penetrate all grid layers, with the standard well model employed to describe well inflow. The modeled trajectory of the deviated producer aligns with the cell orientations, significantly deviating from the actual trajectory, as shown in Fig. 12.

The reference results are expected to be computed by a Cartesian locally refined grid, which features a refined cell size of 2 m $\times$ 2 m $\times$ 2 m for the near-well region, indexed by $14 \leq i \leq 17$, $13 \leq j \leq 16$, and $1 \leq k \leq 10$. Although the modeled well still exhibits a zig-zag shape, the resolution of the trajectory is improved (see Fig. 12).

However, the refined grid does not yield appropriate results in some early stages due to convergence issues. Consequently, a variable size grid is adopted as an alternative to the locally refined grid. In this new grid configuration, the cell sizes in the near-well region remain the same as those in the locally refined grid, and cells with the same index components from the near-well region are replaced with refined cells, as depicted in Fig. 12. While this grid is computationally expensive due to the increased number of cells and faces, it achieves good convergence because all faces are fully matching.

For the NWM hybrid grid, the unstructured grid is constructed within an irregular VOI region. The radial subgrid has angular and radial cell dimensions of 10 and 16, respectively, with a maximum radius of 6 m. The unstructured grid comprises 10 layers, matching the grid layers of the CPG grid. The NWM grid is illustrated in Fig. 13, demonstrating that the modeled well accurately follows its real trajectory.

The black-oil model is utilized to characterize the fluid system, which includes water, free gas, live oil, and dissolved gas. The bubble point pressure is set at 10.4 MPa, and the initial dissolved gas-oil ratio is 62 m^3/m^3. The model is initialized without the presence of free water and free gas, meaning there is no bottom water or gas cap, and all pressures are maintained above the bubble point pressure.

The well operations are divided into two stages. During both stages, the two injectors continuously inject water at a constant rate of 25 m^3/d, while the producer extracts liquids at a constant rate of 50 m^3/d. The primary difference between the two stages lies in the bottom hole pressure limit of the producer: the first stage operates above the bubble point pressure (11 MPa), whereas the second stage falls below the bubble point pressure (5 MPa).

Five simulation cases are presented in this study. The industry-standard simulator Eclipse E100 runs three cases, while the MRST simulator runs two. Fig. 14 reports the comparisons of well solutions, demonstrating that for the same base grid, the results from Eclipse and MRST show a high degree of coincidence. This confirms the accuracy of MRST's underlying simulation functionalities.

Regarding the comparisons between grids, there are no significant differences between the results obtained from the base grid and the three refined grids during the first stage. H-

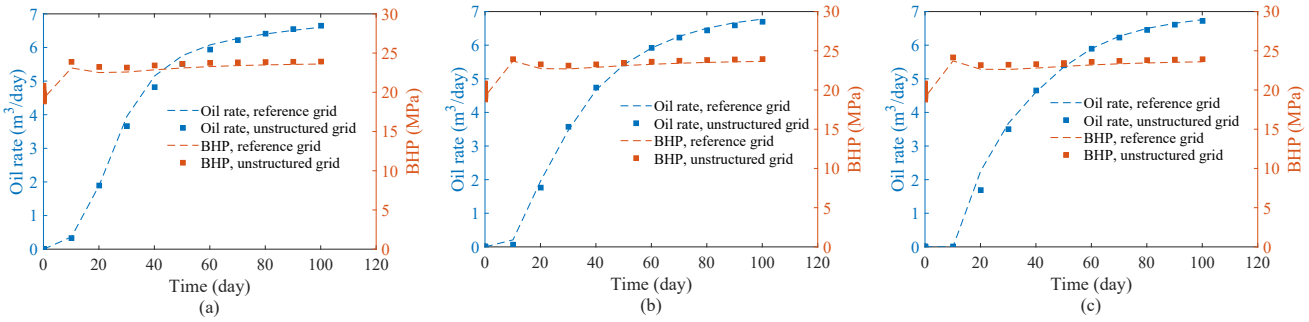

Fig. 11. Comparisons of oil rate and BHP between unstructured grid and fine Cartesian grid for two-phase compressible flow, (a) top surface (2), (b) base surface (4) and (c) bottom surface (7).

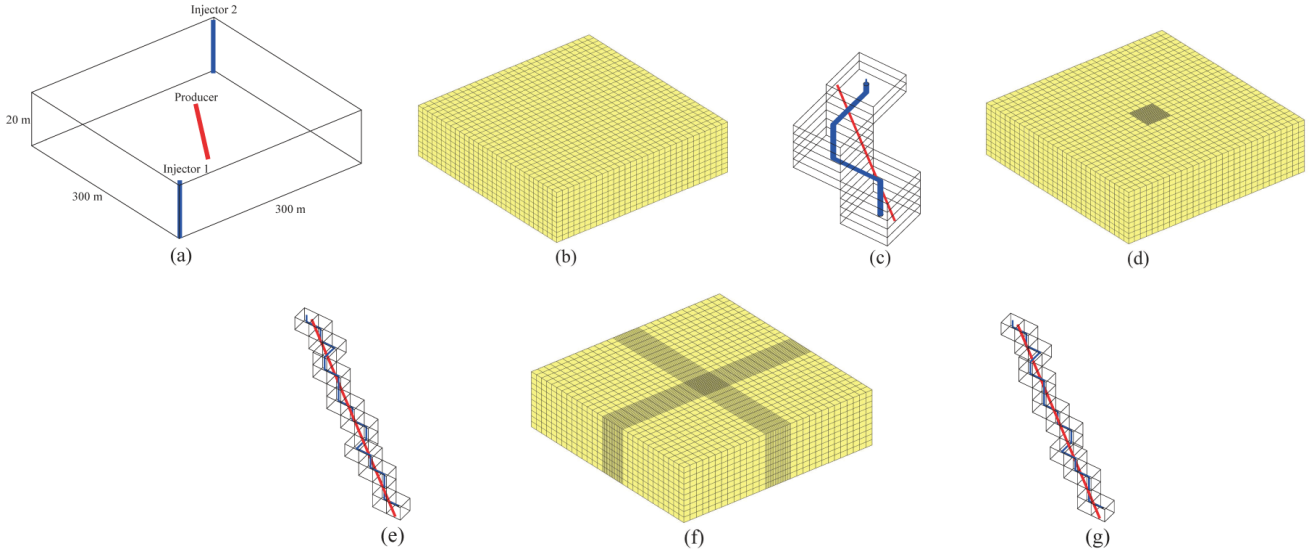

Fig. 12. (a) Well placements, (b) basic Cartesian grid, (c) well cells of basic Cartesian grid, (d) locally refined grid, (e) well cells of locally refined grid, (f) variable size grid and (g) well cells of variable size grid.

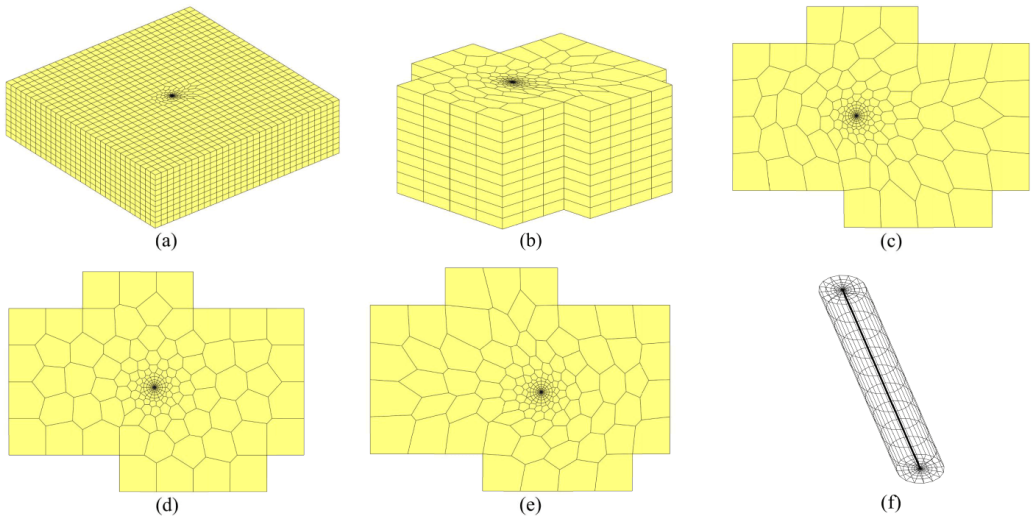

Fig. 13. (a) NWM hybrid grid, (b) layered unstructured grid, (c) surface 2 of layered unstructured grid, (d) surface 6 of layered unstructured grid, (e) surface 10 of layered unstructured grid and (f) radial sub-grid.

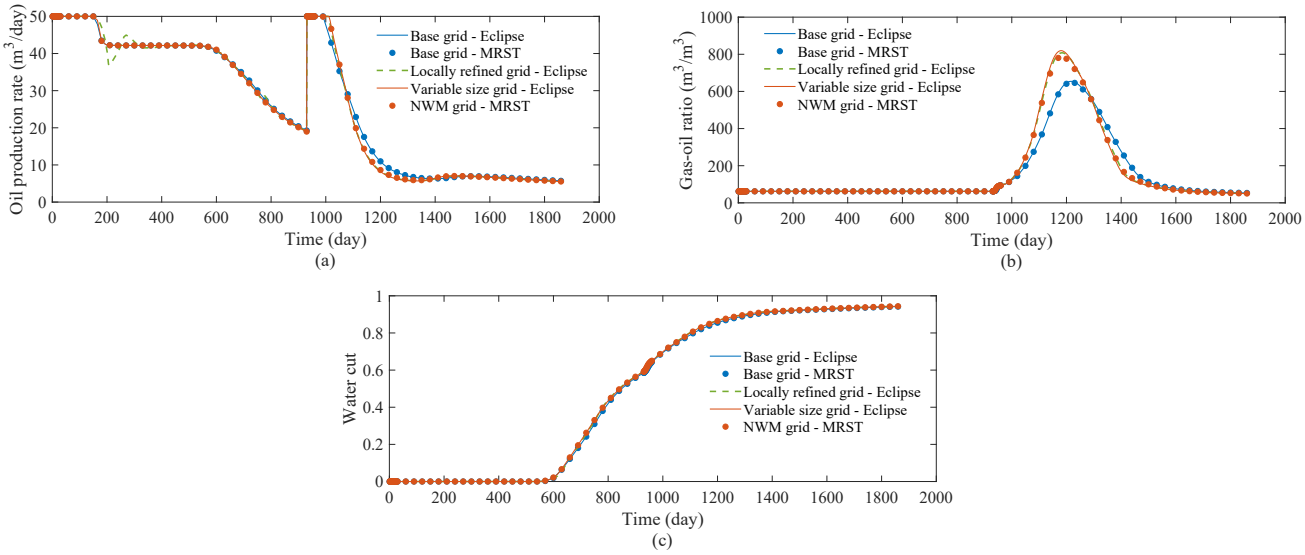

Fig. 14. Comparisons of (a) oil production rate, (b) gas-oil ratio, and (c) water cut between different cases.

Table 1. Number of different grid elements for four grids.

Grid	Numbers			
	Cells	Internal faces	NNCs	Flowing connections
Base	9,000	25,500	0	25,500
Locally refined	12,840	36,156	800	36,956
Variable size	21,160	60,444	0	60,444
NWM	11,330	32,827	280	33,107

owever, in the second stage, while the water cut curves from all four grids remain closely aligned, the oil production rates and gas-oil ratios from the refined grids diverge from those obtained with the base grid. During the first stage, the reservoir experiences a two-phase oil-water flow since no dissolved gas escapes from the oil. In contrast, the second stage exhibits a three-phase black-oil flow as dissolved gas escapes. Consequently, gas flow is more sensitive to grid sizes due to its high compressibility and the complexities of the PVT (pressure-volume-temperature) behavior.

The well solutions obtained from the NMW grid are comparable to those from the locally refined grid and the variable size grid. Gas saturation maps at day 1,110, viewed from different reservoir layers, are presented in Fig. 15. These maps indicate that the results generated by the NMW grid are consistent with those produced by the two refined grids.

Based on the comparisons, the NMW grid demonstrates strong accuracy, providing well solutions and maps that closely align with those obtained from the locally refined grid and variable size grid. The NMW effectively models a high-resolution well trajectory, which is advantageous for property description and further modeling of downhole tools placed at specific depths. Notably, the NMW grid contains only half the number of cells and faces compared to the variable size grid (see Table 1).

Furthermore, the modeling flexibility of the variable size grid is limited for CPG, as the grid input structures (COORD and ZCORN) are challenging to rewrite directly. Although the number of cells and faces in the NMW grid is on par with that of the locally refined grid, the latter may produce unreliable results due to convergence issues, as illustrated by the curves around day 200 in Fig. 14. These convergence problems are exacerbated by higher permeability conditions, as shown in Fig. 16, where the horizontal permeability increases to 0.5 μm^2. In contrast, the NWM grid exhibits good convergence.

6.3 SAIGUP model

A more challenging grid model, the synthetic SAIGUP model (Lie, 2019), is used as an example of a realistic corner-point model. The model dimensions are $40 \times 120 \times 20$, featuring faults, inactive cells, and disconnected components (see Fig. 17). Five vertical injectors and four vertical producers are placed in the reservoir. The target well is a deviated producer located at the center of the reservoir, with an inclination angle of 56°. All injectors penetrate from grid layers 9 to 20, and all producers penetrate layers 1 to 14. For the NWM hybrid grid, an unstructured grid is built within an irregular VOI region (see Fig. 17). The angular and radial cell dimensions of the radial sub-grid are 10 and 20, respectively, with a maximum radius of 30 m. The unstructured grid layers are aligned with the CPG grid layers. The modeled well trajectories from both grids are shown in Fig. 17. It can be observed that the Peaceman model in the CPG produces a zig-zag trajectory, deviating significantly from the actual path, whereas the NWM grid generates a high-resolution trajectory that closely follows the real well path. Herein, the projection model is adopted to enhance the simulation performance for Peaceman model. The well index of a well cell is computed by sub well indices of three directions: $WI = \sqrt{(WI_x)^2 + (WI_y)^2 + (WI_z)^2}$. The sub well index is computed by Peaceman's formulation, and the

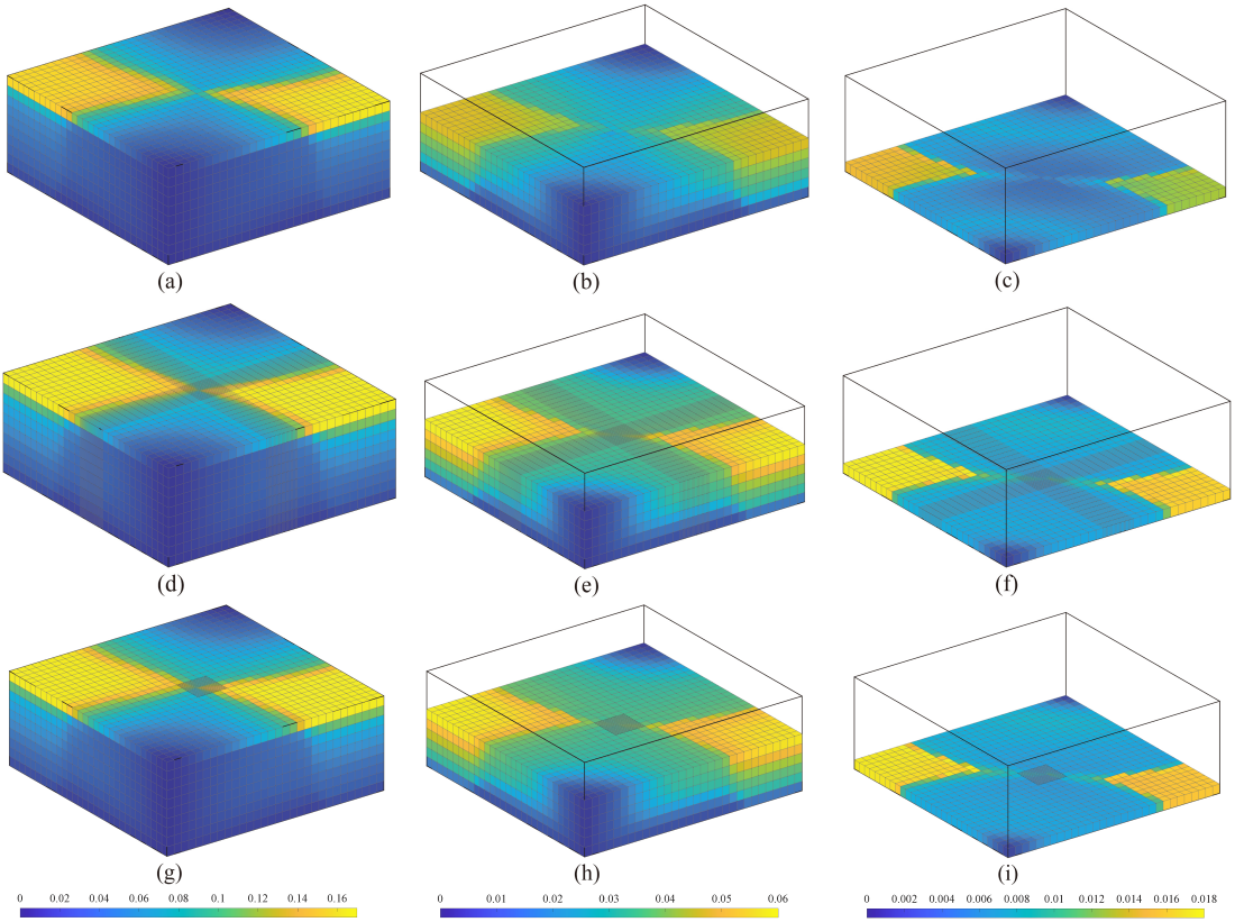

Fig. 15. Comparisons of gas saturation map viewed from different depths between different cases. (a) Basic grid, all layers, (b) basic grid, layer 6-10, (c) basic grid, layer 10, (d) variable size grid, all layers, (e) variable size grid, layer 6-10, (f) variable size grid, layer 10, (g) locally refined grid, all layers, (h) locally refined grid, layer 6-10, (i) locally refined grid, layer 10, (j) NWM grid, all layers, (k) NWM grid, layer 6-10 and (l) NWM grid, layer 10.

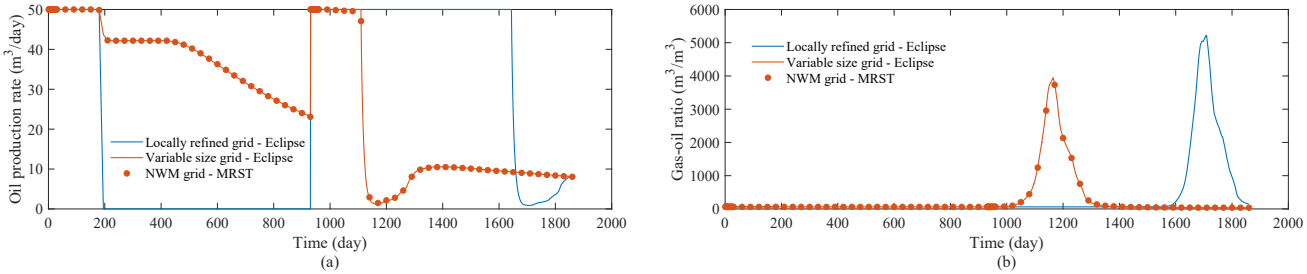

Fig. 16. Comparisons of (a) oil production rate and (b) gas-oil ratio for permeability of 0.5 μm^2.

effective well segment length is given by projection in x, y, or z direction of well segment.

The rock properties exhibit significant heterogeneity, as shown in the logarithmic permeability map in Fig. 18. To improve computational efficiency, an incompressible flow is assumed. The viscosities of oil and water are 5 mPa·s and 1 mPa·s, respectively. A simple Corey relative permeability model is used, with oil and water exponents both set to 2. Residual oil and connate water are neglected. All injectors inject water at a constant rate of 1,000 m^3/d, while all producers operate with a constant bottom-hole pressure, producing liquids at a rate of 10 m^3/d.

Flow computed using the MRST incompressible flow solver, which decouples pressure and transport computations. The well solutions for all producers are shown in Fig. 19. The liquid production rates and water cuts for the four vertical wells (PROD1, PORD3, PROD4, PROD5) are similar between the CPG and NMW grids, as no grid refinements were applied to these wells. Minor deviations highlight the impact of the refined modeling of PROD2 on the flow field. The liquid production rate of PROD2 using the NMW grid is significantly higher than that of the CPG grid, demonstrating the advantage

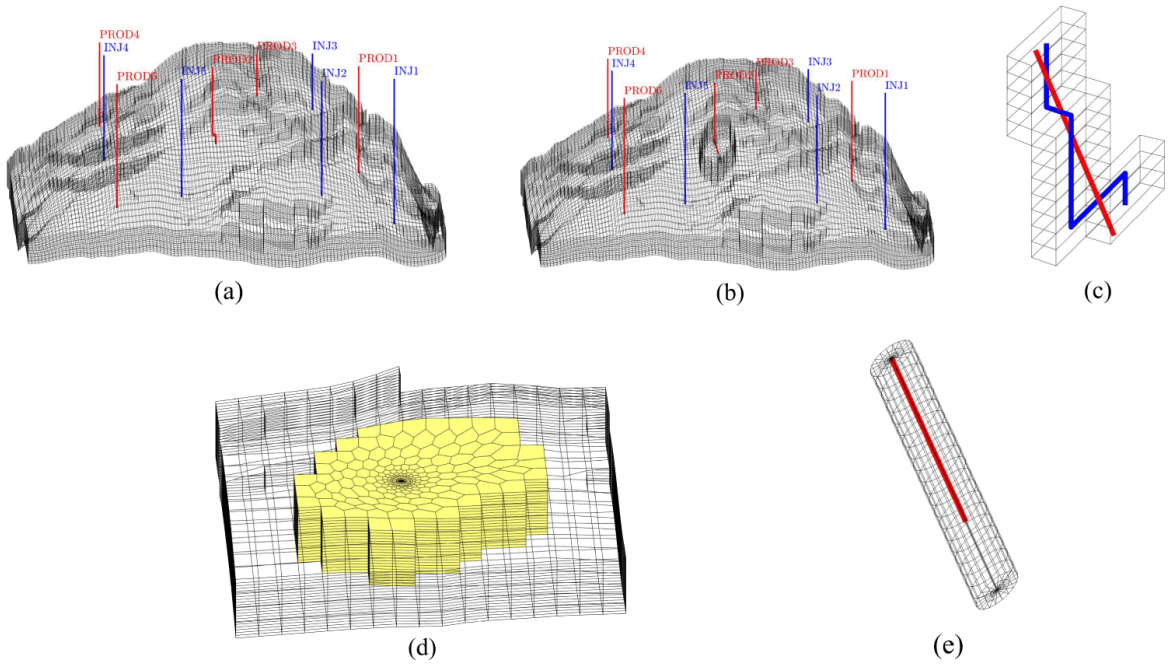

Fig. 17. (a) CPG of SAIGUP model, (b) NWM grid of SAIGUP model, (c) well cells of CPG, (d) unstructured sub-grid of NMW grid and (e) radial sub-grid of NMW grid.

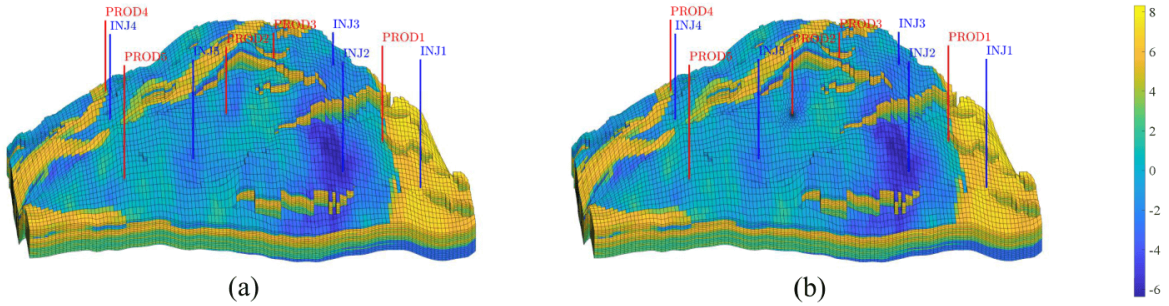

Fig. 18. Map of the logarithm of permeability. (a) CPG and (b) NWM grid.

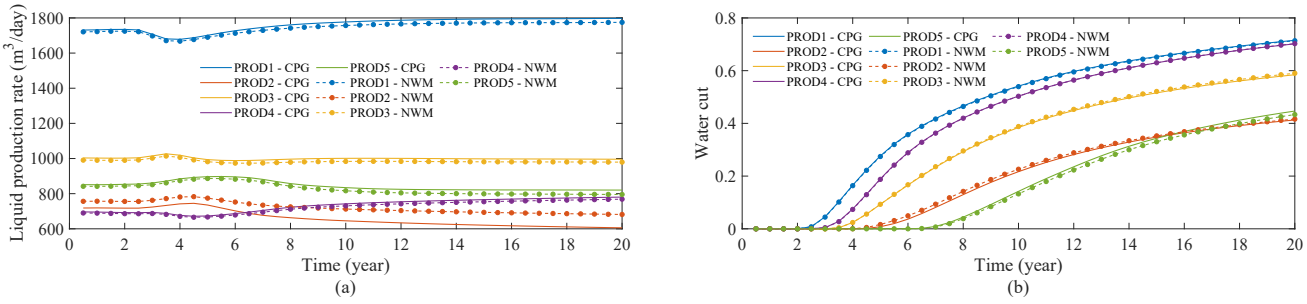

Fig. 19. Plots of (a) oil production rates and (b) water cuts versus time.

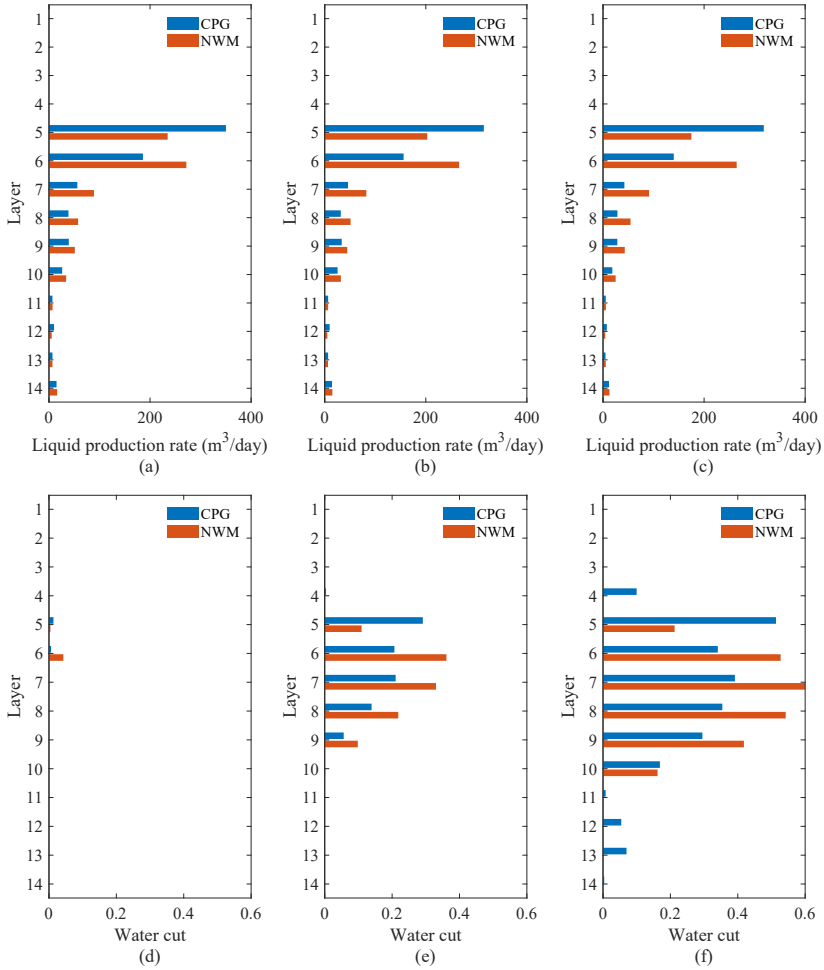

Fig. 20. Oil production rates and water cuts of all penetrated layers at different times. (a) Liquid production rate, 5 year, (b) liquid production rate, 10 year, (c) liquid production rate, 20 year, (d) water cut, 5 year, (e) water cut, 10 year and (f) water cut, 20 year.

of the NMW grid in modeling a deviated well. However, the water cuts for PROD2 are comparable between the NMW and CPG grids, indicating that water cut is less sensitive to grid geometry the water cut is less sensitive to grid geometry compared with gas-oil ratio in homogeneous reservoirs.

The liquid production rates and water cuts for all penetrated layers are presented in Fig. 20. Layer 6, with the highest permeability (see Fig. 21), is expected to produce the most liquids. However, the CPG grid shows the highest liquid production rate in layer 5, whereas the NMW grid provides the correct result, showing layer 6 producing the most liquids. The error in the CPG result stems from the low-resolution trajectory model, which crosses layer 5 with two cells (see Fig. 17). Although the overall well water cuts are similar for the two grids, the water cut distributions across layers differ significantly. For the CPG grid, layer 5 exhibits the highest water cut throughout the production period. The NMW grid, however, offers a more accurate representation of flow physics. At the 5-year mark, layer 6 has the highest water cut, indicating early water breakthrough in the most permeable layer. This is followed by rising water cuts in layers 7 through 10, reflecting subsequent water flow in less permeable layers. By year 20, layer 7 shows the highest water cut, indicating the influence of gravity. Accurate layer-specific predictions of production parameters are critical for enhanced oil recovery operations, where the NMW grid is recommended for more reliable results.

The global and local oil saturation maps at the 10-year mark are shown in Figs. 22 and 23. The global saturation maps generated by both grids are largely similar. However, for the local map, the NMW grid captures the water flow path more accurately, reflecting real flow physics. In contrast, the CPG grid results in a lower-resolution oil saturation map due to its larger grid cell sizes.

Regarding computational efficiency, the simulation time for the CPG grid, which consists of 78,720 cells and 241,613 internal faces, is 108 seconds. In comparison, the NMW grid, with 85,140 cells and 263,672 internal faces plus NNCs, requires 135 seconds. This represents an increase of approximately 9% in the number of cells and faces, and a 25% increase in simulation time. These results demonstrate the NMW grid's potential value for real industry applications, as the computational overhead is acceptable.

As for the gridding efficiency, this example costs 75 s in

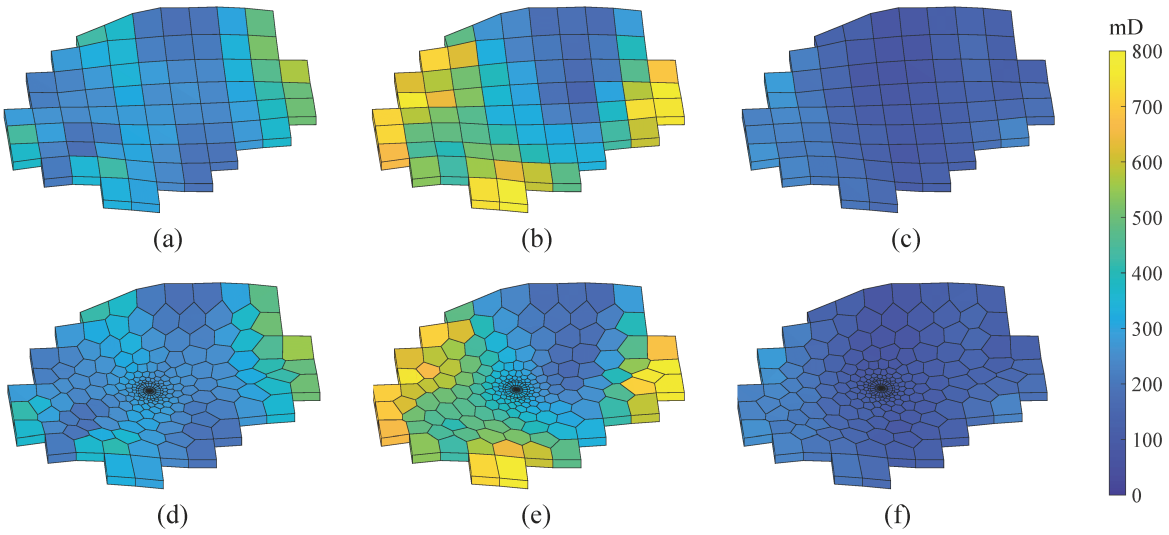

Fig. 21. Permeability map of different layers of VOI region. (a) CPG, layer 5, (b) CPG, layer 6, (c) CPG, layer 7, (d) NWM grid, layer 5, (e) NWM grid, layer 6 and (f) NWM grid, layer 7.

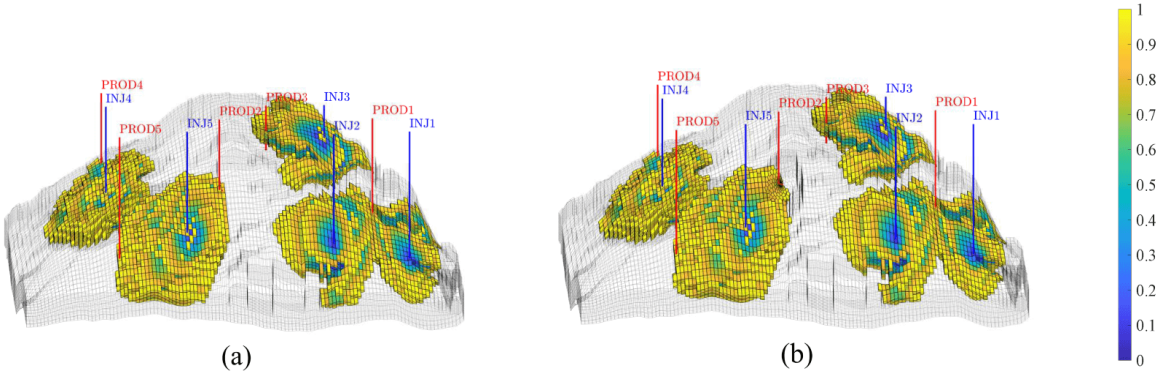

Fig. 22. Oil saturation (< 0.99) maps of two grids at 10-year. (a) CPG and (b) NWM grid.

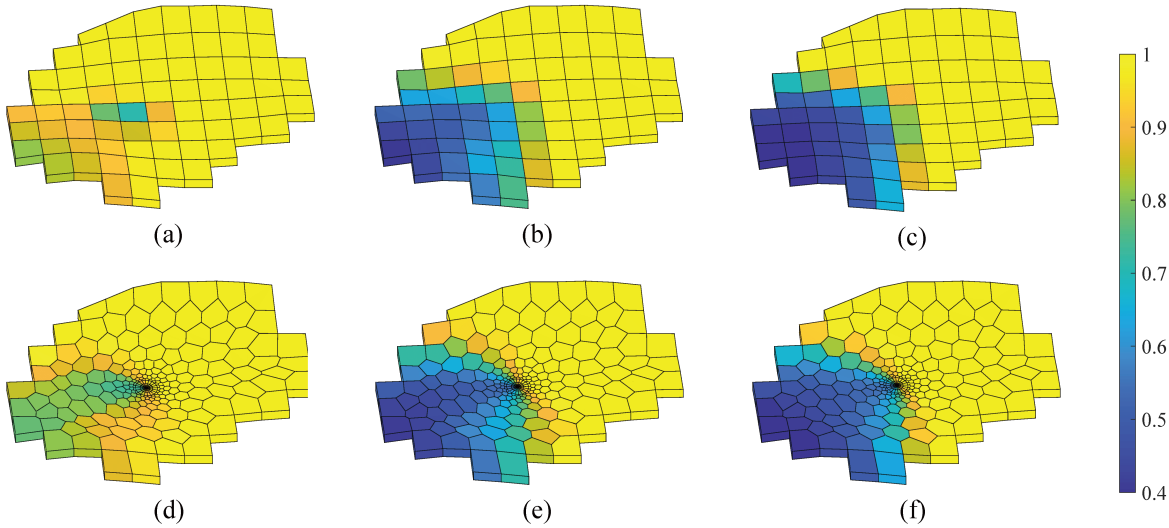

Fig. 23. Oil saturation maps of different layers of VOI region at 10-year. (a) CPG, layer 5, (b) CPG, layer 6, (c) CPG, layer 7, (d) NWM grid, layer 5, (e) NWM grid, layer 6 and (f) NWM grid, layer 7.

gridding process, which is acceptable although the gridding involves several computationally expensive steps. For another, the gridding is performed only once for subsequent simulation studies, e.g., sensitivity analysis, history matching, and production optimization.

7. Concluding remarks

The paper proposes a novel NWM model for deviated wells, featuring a high-quality, robust, hybrid grid and associated simulation routines. The key technical points can be summarized as follows:

1) The new hybrid grid is composed of a CPG that models the far-well region flow and a layered unstructured grid that models the VOI region. The layered unstructured grid includes a radial sub-grid, providing radial resolution for near-wellbore flow, and a Voronoi grid that connects the CPG and radial sub-grid, ensuring fully matched grid connectivity.
2) A flow-based node rearrangement method is introduced to construct 2D grids for all surfaces. In this approach, each node on the target surface shares the same stream and pressure values as its corresponding nodes on the base surface. The method involves solving the incompressible pressure equation numerically, tracing streamlines using Pollock's algorithm, and executing a series of 2D interpolations.
3) The simulation examples demonstrate that the new NWM model yields well solutions and maps that closely align with reference results, all while maintaining a manageable computational cost.
4) For scenarios involving gas flow with high compressibility and complex PVT physics, the NWM model is recommended for its ability to reliably predict physics flow in heterogeneous reservoirs and assess production parameters across layers, thereby supporting further enhanced oil recovery operations.

Acknowledgements

We gratefully thank the Applied Computational Sciences group at SINTEF Digital for providing the open-source reservoir simulation software MRST. We gratefully acknowledge the financial support of General Program of National Natural Science Foundation of China (No. 52374055).

Supplementary file

https://doi.org/10.46690/ager.2025.02.04

Conflict of interest

The authors declare no competing interest.

References

Abou-Kassem, J. H., Aziz, K. Analytical well models for reservoir simulation. Society of Petroleum Engineers Journal, 1985, 25(4): 573-579.

Aziz, K., Settari, A. Petroleum reservoir simulation. Applied Science Publishers, 1979.

Bennis, C., Borouchaki, H., Flandrin, N. Hybrid mesh generation for local grid refinement in reservoir flow simulation. Paper Presented at 10th European Conference on the Mathematics of Oil Recovery, Amsterdam, 4-7 September, 2006.

Bennis, C., Borouchaki, H., Flandrin, N. 3D conforming power diagrams for radial LGR in CPG reservoir grids. Engineering with Computers, 2008, 24: 253-265.

Berge, R. L., Klemetsdal, Ø. S., Lie, K. A. Unstructured Voronoi grids conforming to lower-dimensional objects. Computational Geosciences, 2019, 23: 169-188.

Ding, D. Y. Coupled simulation of near-wellbore and reservoir models. Journal of Petroleum Science and Engineering, 2011, 76: 21-36.

Ding, S., Jiang, H., Li, J., et al. Optimization of well placement by combination of a modified particle swarm optimization algorithm and quality map method. Computational Geosciences, 2014, 18(5): 747-762.

Ding, Y., Renard, G., Weill, L. Representation of wells in numerical reservoir simulation. SPE Reservoir Evaluation & Engineering, 1998, 1(1): 18-23.

Dogru, A. H. Equivalent wellblock radius for partially perforated vertical wells-Part I: Anisotropic reservoirs with uniform grids. SPE Journal, 2010a, 15(4): 1034-1043.

Dogru, A. H. Equivalent wellblock radius for partially perforated vertical wells-Part II: Anisotropic heterogeneous reservoirs with nonuniform grids. SPE Journal, 2010b, 15(4): 1038-1046.

Ewing, R. E., Boyett, B. A., Babu, D. K., et al. Efficient use of locally refined grids for multiphase reservoir simulation. Paper SPE 18413 Presented at SPE Symposium on Reservoir Simulation, Houston, Texas, 6-8 February, 1989.

Flandrin, N., Borouchaki, H., Bennis, C. 3D hybrid mesh generation for reservoir flow simulation. Paper Presented at 9th European Conference on the Mathematics of Oil Recovery, Cannes, 30 August-2 September, 2004.

Flandrin, N., Borouchaki, H., Bennis, C. 3D hybrid mesh generation for reservoir simulation. International Journal for Numerical Methods in Engineering, 2006, 65: 1639-1672.

GeoQuest. ECLIPSE reference manual 2021.1. Schlumberger, 2021.

Hoteit, H., Chawathé, A. Making field-scale chemical enhanced-oil-recovery simulations a practical reality with dynamic gridding. SPE Journal, 2016, 21(6): 2220-2237.

Krogstad, S., Durlofsky, L. J. Multiscale mixed-finite-element modeling of coupled wellbore/near-well flow. SPE Journal, 2009, 14(1): 78-87.

Krogstad, S., Lie, K. A., Møyner, O., et al. MRST-AD - An open-source framework for rapid prototyping and

evaluation of reservoir simulation problems. Paper SPE 173317 presented at SPE Reservoir Simulation Symposium, Houston, Texas, 23-25 February, 2015.

Lie, K. A. An Introduction to Reservoir Simulation Using MATLAB/GNU Octave: User Guide to the MATLAB Reservoir Simulation Toolbox (MRST). Cambridge, UK, Cambridge University Press, 2019.

Lie, K. A., Krogstad, S., Ligaarden, I. S., et al. Open-source MATLAB implementation of consistent discretisations on complex grids. Computational Geosciences, 2012, 16: 297-322.

Mouton, T., Bennis, C., Borouchaki, H. Hybrid mesh generation for reservoir flow simulation in CPG grids. Paper Presented at the 18th International Meshing Roundtable, Salt Lake City, UT, 25-28 October, 2009.

Mouton, T., Borouchaki, H., Bennis, C. Hybrid mesh generation for reservoir flow simulation: Extension to highly deformed corner point geometry grids. Finite Elements in Analysis and Design, 2010, 46(1-2): 152-164.

Peaceman, D. W. Interpretation of well-block pressures in numerical reservoir simulation. Society of Petroleum Engineers Journal, 1978, 18(3): 183-194.

Peaceman, D. W. Interpretation of well-block pressures in numerical reservoir simulation with nonsquare grid blocks and anisotropic permeability. Society of Petroleum Engineers Journal, 1983, 23(3): 531-543.

Peaceman, D. W. Interpretation of wellblock pressures in numerical reservoir simulation part 3 - Off-center and multiple wells within a wellblock. SPE Reservoir Engineering, 1990, 5(2): 227-232.

Pedrosa, O. A., Aziz, K. Use of hybrid grid in reservoir simulation. SPE Reservoir Engineering, 1986, 1(6): 611-621.

Persson, P. O. Mesh generation for implicit geometries. Cambridge, Massachusetts Institute of Technology, 2005.

Persson, P. O., Strang, G. A simple mesh generator in MATLAB. SIAM Review, 2004, 46(2): 329-345.

Pollock, D. W. Semi-analytical computation of path lines for finite-difference models. Ground Water, 1988, 26(6): 743-750.

Ponting, D. K. Corner point grid geometry in reservoir simulation. Paper Presented at the 1st European Conference on Mathematics in Oil Recovery, 14-16 July, 1989.

Rosenberg, D. U. Local mesh refinement for finite difference methods. Paper SPE 10974 presented at SPE Annual Technical Conference and Exhibition, New Orleans, LA, 26-29 September, 1982.

Su, H. J. Modeling off-center wells in reservoir simulation. SPE Reservoir Engineering, 1995, 10(1): 47-51.

Wang, Y., Shahvali, M. Discrete fracture modeling using centroidal Voronoi grid for simulation of shale gas plays with coupled nonlinear physics. Fuel, 2016, 163: 65-73.

Zhao, L., Jiang, H., Wang, H., et al. Representation of a new physics-based non-Darcy equation for low-velocity flow in tight reservoirs. Journal of Petroleum Science and Engineering, 2020, 184: 106518.

Zhao, L., Jiang, H., Zhang, S., et al. Modeling vertical well in field-scale discrete fracture-matrix model using a practical pseudo inner-boundary model. Journal of Petroleum Science and Engineering, 2018, 166: 510-530.